Published online 8 November 2018 *Nucleic Acids Research, 2018, Vol. 46, No. 22* ***11687–11697***
doi: 10.1093/nar/gky1082

Effect of *in vivo* post-translational modifications of the HMGB1 protein upon binding to platinated DNA: a molecular simulation study

Wenping Lyu (Lv)[1,2,3], Fabio Arnesano[4], Paolo Carloni[1,*], Giovanni Natile[4,*] and Giulia Rossetti[1,5,6,*]

[1]Computational Biomedicine, Institute for Advanced Simulation IAS-5 and Institute of Neuroscience and Medicine INM-9, Forschungszentrum Jülich, 52425 Jülich, Germany, [2]Faculty of Mathematics, Computer Science and Natural Sciences, RWTH-Aachen University, 52056 Aachen, Germany, [3]Computation-Based Science and Technology Research Center, Cyprus Institute, 2121 Aglantzia, Nicosia, Cyprus, [4]Department of Chemistry, University of Bari "A. Moro", via Edoardo Orabona 4, 70125 Bari, Italy, [5]Department of Hematology, Oncology, Hemostaseology, and Stem Cell Transplantation, Faculty of Medicine, RWTH Aachen University, 52062 Aachen, Germany and [6]Jülich Supercomputing Centre (JSC), Forschungszentrum Jülich, 52425 Jülich, Germany

Received May 01, 2018; Revised October 11, 2018; Editorial Decision October 12, 2018; Accepted October 19, 2018

ABSTRACT

Cisplatin is one of the most widely used anticancer drugs. Its efficiency is unfortunately severely hampered by resistance. The High Mobility Group Box (HMGB) proteins may sensitize tumor cells to cisplatin by specifically binding to platinated DNA (PtDNA) lesions. *In vivo,* the HMGB/PtDNA binding is regulated by multisite post-translational modifications (PTMs). The impact of PTMs on the HMGB/PtDNA complex at atomistic level is here investigated by enhanced sampling molecular simulations. The PTMs turn out to affect the structure of the complex, the mobility of several regions (including the platinated site), and the nature of the protein/PtDNA non-covalent interactions. Overall, the multisite PTMs increase significantly the apparent synchrony of all the contacts between the protein and PtDNA. Consequently, the hydrophobic anchoring of the side chain of F37 between the two cross-linked guanines at the platinated site—a key element of the complexes formation - is more stable than in the complex without PTM. These differences can account for the experimentally measured greater affinity for PtDNA of the protein isoforms with PTMs. The collective behavior of multisite PTMs, as revealed here by the synchrony of contacts, may have a general significance for the modulation of intermolecular recognitions occurring *in vivo*.

INTRODUCTION

Cisplatin, or *cis*-diamminedichloridoplatinum(II), is a major anticancer drug in the treatment of several solid tumors (1–5). Cisplatin induces cell death by binding to DNA and inhibiting replication and transcription (1). Unfortunately, drug efficiency is severely limited by resistance mechanisms (6,7), either intrinsic or developed by tumor cells after an initial sensitivity (8). The d(GpG) and d(ApG) intrastrand cross-links (9) account for about 90% of the cisplatin–DNA lesions formed *in vivo* (9–11). The distorted DNA is recognized and forms adducts with chromosomal non-histone nucleoproteins containing the High Mobility Group Box (HMGB), e.g. HMGB1 and HMGB4 (12,13). This is a pharmaceutically relevant event, since it can inhibit the cisplatin–DNA damage repair (12) and favor tumor-cell death (14,15). A correlation between higher binding affinity of HMGB proteins toward cisplatin–DNA lesions and lower DNA-repair efficiency has been observed in various instances (12,15–18).

The structural determinants of the major complex between HMGB1 box-A and platinated DNA ($[Pt(NH_3)_2]^{2+}$-*d*(CCUCTCTG*G*ACCTTCC)-d(GGAGAGACCTGGAAGG), PtDNA) have been revealed by a fundamental X-ray study of Lippard and co-workers (19). Beside this major intrastrand adduct, the

*To whom correspondence should be addressed. Email: p.carloni@fz-juelich.de
Correspondence may also be addressed to Giovanni Natile. Email: giovanni.natile@uniba.it
Correspondence may also be addressed to Giulia Rossetti. Email: g.rossetti@fz-juelich.de

drug can form also interstrand adduct with DNA (20). Here, the protein binds to the PtDNA from the minor groove using non-covalent interactions (21) contemplating also a key insertion of the phenyl ring of F37 into a hydrophobic notch created by the two cross-linked guanines at the damaged site (19). The relevance of this complex *in vivo* is challenging since several post-translational modifications (PTMs), including lysine acetylation and serine phosphorylation at multiple sites (22), can modulate the binding affinity of HMGB1 isoforms for PtDNA (22–28). PTMs have been defined as covalent modifications of amino-acid residues in proteins (29) that allow the hydrophobicity and other physico-chemical properties of the protein to be tuned for specific biological functions (30,31). For instance, a single-site lysine acetylation is known to affect the interaction with DNA of H3 histone (32), while multisite acetylation of the H4 histone tail introduces both specific and cumulative effects on the protein conformation (33).

Acetylation of lysine and phosphorylation of serine both reduce positive charges on HMGB1 protein, hence one may expect a decreased electrostatic attraction for the negatively charged DNA (34,35). This is for instance the case of a widely studied complex, the nuclear factor-κB (NF-κB)/DNA complex (36,37), where multisite lysine acetylation markedly decreases the binding affinity for DNA (38). However, this instinctive assumption conflicts with the binding affinities measured experimentally for the HMGB1/PtDNA complexes (22–28) where the mixture of four *in vivo* HMGB1 isoforms (22) turned out to bind PtDNA with greater affinity than the protein without PTMs. A plausible explanation for these observations was that the conformational changes induced by the PTMs, rather than the charge, affect the binding of HMGB1 to PtDNA (22,23). Unlike the case of widely-investigated interactions between proteins and small molecules, in the HMGB1/PtDNA complex the rugged intermolecular interface involves many interfacial contacts building up a complex interaction network. How multisite PTMs can affect this kind of interaction network has not yet been explored.

Molecular dynamics (MD) simulations can give insight into the atomistic level of the molecular recognition interfaces and has already been successfully applied to some biosystems including cytotoxic metallodrugs and their targets (39,40). Combining MD simulations and experimental evidences, the target preferences of several promising transition metal anticancer agents (41–45), such as platinum- and ruthenium-based compounds, have been elucidated.

In this work, we address the issue of multisite PTMs by enhanced sampling atomistic molecular simulations of the four known PTM isoforms (22) starting from the X-ray structure of the isoform without PTMs (19). We investigated both the structural properties of the complexes and the collective behaviors originating from multisite PTMs. The collective behaviors were investigated in terms of 'synchrony' in the formation of the non-covalent interactions between protein and PtDNA. In other words, given a pair of intermolecular direct contacts A and B, we investigated whether A is formed simultaneously to B, and how will this synchrony of contact be modulated by different *in vivo* PTMs patterns.

Anticipating our results, the PTMs turned out to affect the nature of the intermolecular contacts and to change the conformational fluctuations not only of specific regions, but also of the overall complex. In all cases, the PTMs render the interactions between protein and PtDNA more synchronic.

MATERIALS AND METHODS

Calculation details

The resolved X-ray structure of HMGB1 in complex with platinated DNA ($[Pt(NH_3)_2]^{2+}$–*d*(CCUCT CTG*G*ACCTTCC)–*d*(GGAGAGACCTGGAAGG)) covers the box-region A from residue 8 to 78 (PDBID 1CKT (19)). To cover as much as possible the experimentally observed *in vivo* PTMs (22), we included in our simulations the N'-tail and the box-linker (Supplementary Figure S1 in supporting information (SI), from homology modeling based on a full-length structure of HMGB1 (PDBID: 2YRQ)), called **noPTM** hereafter. The *in vivo* PTM patterns reported in previous work (22) (**A**, **B**, **C** and **D**, Table 1) are added to **noPTM** using an in-house code. Next, 100-ns long MD simulation based on the AMBER ff99SB-ILDN (46–48) and Parmbsc1 (49) force fields was carried out for the following five systems: cisplatin–DNA (**PtDNA**) bound to the HGMB1 box A (HGMB1A hereafter) without PTM (**noPTM**) or to HGMB1A isoforms **A**, **B**, **C** and **D**. Then, replica exchange with solute scaling sampling simulations (50) were carried out on these complexes (*i.e.* **PtDNA•A**, **PtDNA•B**, **PtDNA•C** and **PtDNA•D**, as well as **PtDNA•noPTM**). Five more systems were built as follows. The proteins present in the replicas of the five complexes (before enhanced sampling) were inserted in a box of the same size as that used in the complexes simulations. Each protein box was filled with 0.15 M NaCl in water, as used in the complexes simulations (see Supplementary Table S8). The same enhanced sampling condition as for the complexes was then applied to each one of these systems. Technical details of the homology modeling, MD system setups, enhanced sampling simulations, and simulation parameters are reported in SI.

Conformational analyses

The bending of **PtDNA** and the opening of paired bases as well as other helical parameters were calculated using Curves+ (51). The hydrogen bonds and the non-bonded contacts were calculated based on the contacts list generated from HBPLUS (52) and NUCPLOT (53). Direct or water-mediated hydrogen bonds were identified with the following criteria: Hydrogen (H)–acceptor (A) distance <2.7 Å, donor (D)–A distance <3.35 Å, D–H–A angle >90°. **PtDNA**–protein hydrophobic interactions were assumed for distances between atom pairs of 3.9 Å or smaller. Herein, only hydrophobic side chains or polar/charged side chains not involved in direct or water mediated H-bonds and/or salt bridges were considered. The electrostatic contacts (salt-bridges) are the non-bonded contacts between positively charged protein residues and phosphate groups of **PtDNA**. The stacking contacts are the non-bonded contacts between aromatic residues and nucleobases. All the rest of

Table 1. PTM sites in the four *in vivo* HMGB1 isoforms (**A–D** in Figure 1)

	Acetylated lysine	Phosphorylated serine	Number of PTM sites
A	K11, K29, K42, K75, K81, K89	–	6
B	K2, K11, K29, K42, K54, K58, K81, K85, K89	–	9
C	K11, K54, K81, K89	S14, S34, S52	7
D	K11, K29, K42, K81, K87	S34	6

non-bonded contacts are considered as van der Waals contacts. Before further processing, noisy intermolecular contacts have been filtered out to guarantee 95% confidence interval by bootstrap resampling (Supplementary Figure S2).

Conformational entropy analyses

The change of conformational entropy upon the binding of the proteins to **PtDNA** was estimated by quasi-harmonic approximation (54,55). The representative structures of each solute (protein-**PtDNA** complexes, free states of the proteins and **PtDNA**) were described as a disjoint multidimensional harmonic well (56), by which the conformational entropy is connected to the change in internal structural dynamics (55). The entropy from fast intra-well motion of the solute was estimated by the quasi-harmonic approximation (54,55).

Synchrony of contacts

For synchrony analysis, we need to define several quantities. The *effective number of contacts* ($w_{f,i}$) is the number of direct contacts (i.e. not water mediated contacts) between residue i and **PtDNA** at the simulation snapshot f, divided by the number of all such contacts:

$$w_{f,i} = \frac{\sum_{a\in N_i}\sum_{b\in D}\delta^f_{a,b}}{\sum_{a\in N}\sum_{b\in D}\delta^f_{a,b}} \quad (1)$$

N, N_i and D are the number of atoms of the protein, that of the residue i, and that of **PtDNA**, respectively. $\delta^f_{a,b}= 1$ if atom a and atom b are in contact, $\delta^f_{a,b} = 0$ otherwise. $\sum_{a\in N_i}\sum_{b\in D}\delta^f_{a,b}$ is the number of contacts of residue i at snapshot f. $\sum_{a\in N}\sum_{b\in D}\delta^f_{a,b}$ is the number of contacts of all residues at snapshot f.

The *pairwise synchrony* ($P_{i,j}$) between two residues i and j is defined as the normalized sum of $w_{f,i}\cdot w_{f,j}$ over all considered simulations snapshots M:

$$P_{i,j} = \frac{\sum_{f=1}^{M} w_{f,i}w_{f,j}}{\sqrt{(\sum_{f=1}^{M} w_{f,i}{}^2)(\sum_{f=1}^{M} w_{f,j}{}^2)}} \quad (2)$$

$P_{i,j}$ ranges between 0 and 1. If $P_{i,j}= 1$, **PtDNA**–protein contacts of two residues i and j are formed simultaneously for all M snapshots (fully synchronic residues pairs). $P_{i,j} = 0$ if this is never the case. Partially synchronic pairs are defined if $0.5 < P_{i,j} < 1$. Here, the residues forming partially and/or fully synchronic pairs are represented as linked nodes (with edges) in a network (the *synchronic network*). The latter can be conveniently characterized by the *synchrony index* I:

$$I = \Sigma_{i,j\in \boldsymbol{R},\ i\neq j,\ \ P_{i,j}>0.5} P_{i,j} / \Sigma_{i,j\in \boldsymbol{R},\ i\neq j,\ \ P_{i,j}>0.5} A \quad (3)$$

Here, $A = 1$. $\boldsymbol{R}$ includes all R nodes of the synchronic network. I is the sum of the pairwise synchronies of all (partially and fully) synchrony nodes in a synchronic network divided by the number of edges between linked nodes. The latter corresponds to a fully synchronic network with the same topology as the calculated one. This ensures that the synchrony index can be used to compare the overall synchronies across different systems: the difference of the topology of different networks is canceled out.

Next, we notice that the synchronic network can be regrouped into one or more *synchronic subgroups*; in each *subgroup*, all nodes are synchronous to one node (the *synchronic center*) and they may well be also synchronous to each other. There is a very large number of possible subdivisions in subgroups. Here, we identify the subdivision that minimizes the so-called *Bethe free energy* (57), following an established procedure (58). To this aim, we maximize a quantity – the *net synchrony* S(L)– that is anticorrelated to the *Bethe free energy* (57). $L = (L1,\ldots, L_R)$ is a set of labels which allows us to distinguish the synchronic subgroups: (58) $L_i = k$ when node k is the synchronic center of node i. For instance, $L_2 = 4$ means that the node 4 is the synchronic center of node 2. Thus, necessarily $L_k = k$: the node k must be the synchronic center of itself.

S(L) reads: (58)

$$\mathrm{S}(L) = \sum_{i=1}^{\mathrm{R}} P_{i,L_i} + \text{penalty term} \quad (4)$$

Here, the penalty term equals $-\infty$ if the required conditions above ($L_i = k$, $L_k = k$) are not satisfied at the same time. S(L) is maximized by using the *affinity propagation algorithm* (58) (see SI for details).

To visualize the subgroups and the synchronic networks, we found convenient to project them onto a 2D space. In this way, nodes involved in (a)synchronic contacts are located relatively (far) close to each other (59–61). This is done by performing a standard multidimensional scaling procedure: principal coordinates analysis (59–61). The synchrony code is available upon request from the authors.

RESULTS AND DISCUSSION

The present investigation comprises the four PTM-bearing HMGB1 box-A isoforms (22) (**A-D** hereafter, see Table 1) detected *in vivo* in complex with the platinated DNA (**PtDNA** hereafter). These feature 4–9 acetylated lysine and 0–3 phosphorylated serine residues (Table 1) (22). Comparison is made with the isoform without PTM in complex with the platinated DNA (**PtDNA•noPTM**). The **PtDNA•A-D** and **PtDNA•noPTM** complexes underwent 100-ns long

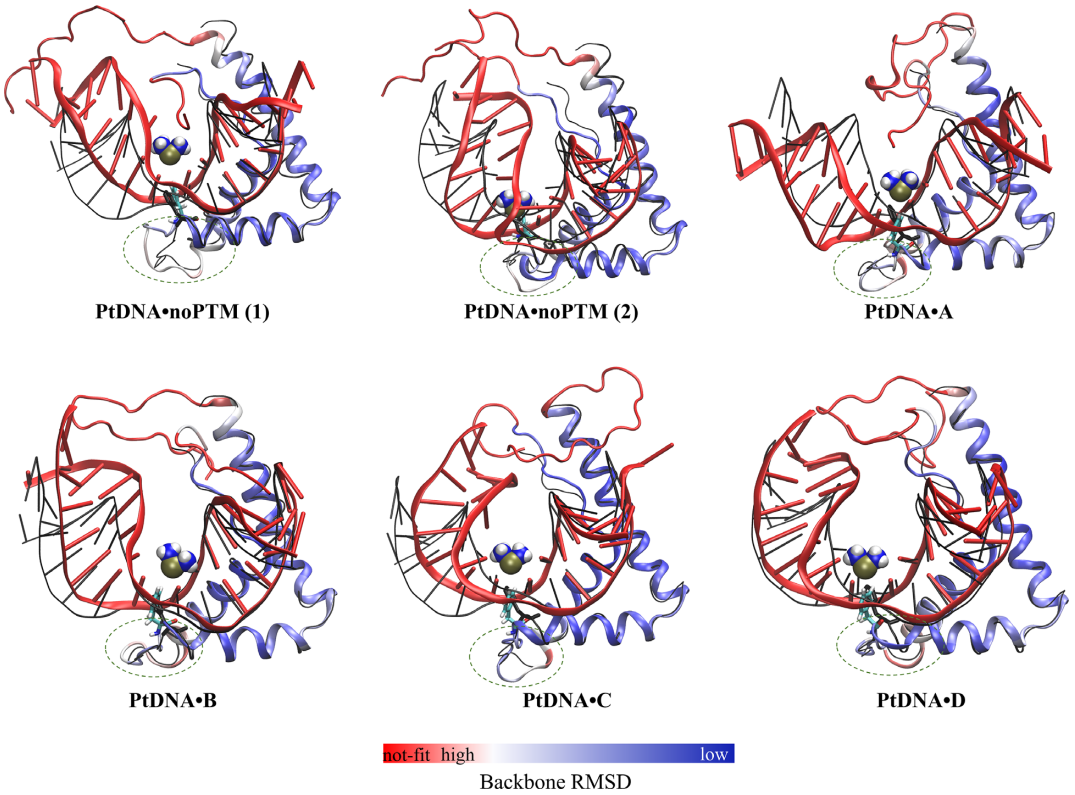

Figure 1. Most populated structures of the five complexes investigated here emerging from our enhanced sampling simulations. **PtDNA•noPTM(1)** and **PtDNA•noPTM(2)** are both significantly populated structures of the isoform without PTMs. The X-ray structure of the isoform without PTMs (9) is depicted in a 'black thin line' representation. The major groove is directed to north and the minor groove to south. The loops connecting the proteins' α-helixes 1 and 2 are inscribed in dotted-line circles. The protein is colored from blue to red (see bar at the bottom of the Figure) according to the backbone RMSD relative to the X-ray structure. The **PtDNA** is colored in red. F37 (sticks) and $[Pt(NH_3)_2]^{2+}$ (van der Waals spheres) are colored according to the atomic codes: N, blue; H, white; Pt, gold; C, cyan.

Hamiltonian replica exchange enhanced sampling simulations (50) with 16 replicas. To improve sampling efficiency, care was taken to reduce memory effects and to increase swapping efficiencies across replicas (Supplementary Figure S3). The conformations generated in the first 50 ns were discarded based on a convergence analysis reported in SI (see *Simulations* in Materials and Method section and Supplementary Figure S4).

More than ten structural representatives of each system were identified by a cluster analysis (see Supplementary Figures S5 and S6). The first ten representatives cover most (90–99%) of the conformational space of each system (Supplementary Figure S6). Figure 1 presents the highly-populated structures of each system and their backbone deviation (*i.e.* standard deviation of each residue) relative to the X-ray structure.

Structural properties and conformational fluctuations

The protein. The helical secondary structure of the protein is well conserved during the simulations (Supplementary Table S1). The root-mean-square deviation (RMSD) of the protein backbone relative to that of the X-ray structure is ∼1.6 Å (Supplementary Table S2). The major contribution comes from residues nearby the terminal regions and the loop connecting the α-helixes 1 and 2 (inscribed in dotted-line circles in Figure 1). Changes within the three α-helixes domains (box-region), corresponding to changes in the proteins' 'L-shape', are characterized in terms of inter-helical spatial angles α, β, and γ (Figure 2A). Similarity with the X-ray structure is observed for the 'L-shapes' of **A**, **B**, and **D** (Figure 2A); whereas, with respect to the X-ray structure, β is increased and γ is decreased for **noPTM** and **C**, indicating a slightly larger bending toward the **PtDNA**.

Compared to the box-region, the two protein terminals experience much greater (>2-fold) root-mean-square fluctuations (RMSFs) (Supplementary Table S3). This is not unexpected for such unstructured loops (28). More interesting is the fact that the terminals' RMSFs decrease on passing from **noPTM** (∼0.8 Å) to the four PTM isoforms (∼0.3–0.5 Å, Supplementary Table S3). Consistent with a larger flexibility of **noPTM** relative to **A–D**, **noPTM** features two main structures in solution, whereas the other isoforms feature only one structure (Figure 1). We conclude that major differences between **noPTM** and **A–D** are due to the conformational fluctuations of the proteins' terminals.

The PtDNA. The platinated DNA preserves its double helix structure across the five adducts (Supplementary Figure S5). However, it undergoes more significant overall rearrangements than the protein molecule, with the RMSD of the **PtDNA** backbone ranging from 3.3 to 6.1 Å (Supplementary Table S2). The conformation of the **PtDNA** was

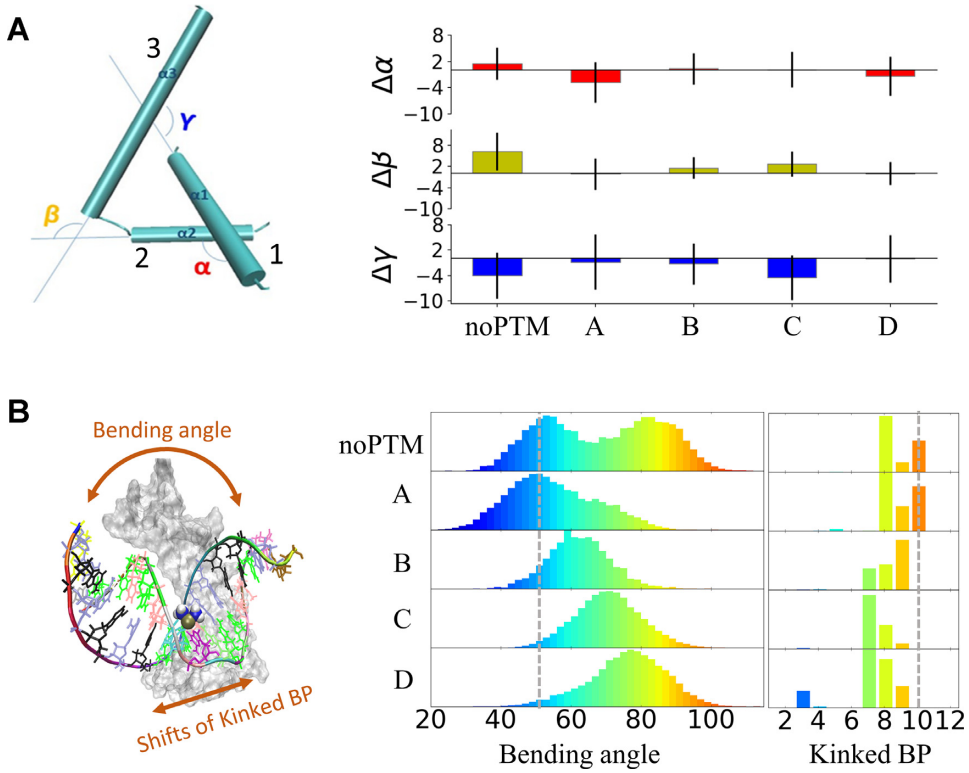

Figure 2. (**A**) Conformation of the helices in the box-region. Left: definition of the inter-helical spatial angles (α, β and γ). Right: histogram showing deviations of α, β and γ relative to the X-ray structure (α = 115°, β = 114° and γ = 117°); error bars indicate the standard deviations. (**B**) Distributions of bending angle and shifts of kinked base-pair (Kinked BP). Left: graphical representation of bending angle and shifts of Kinked BP. Right: distribution of bending angle and Kinked BP shifts of the platinated DNA. Distributions from lower to higher values are colored spanning from blue to red. Bending angle and Kinked BP of the X-ray structure are marked as grey dot lines.

characterized in terms of: (i) bending angle, calculated as sum of the individual bending angles of the inter-base axis (51,62) (this corresponds to the overall bending of **PtDNA**) and (ii) kinked base pair (Kinked BP), that is the base pair step where the maximum bending of the inter-base axis occurs (63,64) (it corresponds to the point of kinking of **PtDNA**) (Figure 2B).

The **PtDNA**'s bending angle ranges from ∼30° to ∼100°, with bi- and uni-modal distributions in **PtDNA•noPTM** and in **PtDNA•A-D**, respectively (Figure 2B). Similar distributions of the so-called helix axes subtending angle (65), which may be employed to characterize the overall bending of the **PtDNA** (65), are observed for **PtDNA•noPTM** and **PtDNA•A-D** (Supplementary Figure S7). The Kinked BP is located at base pair step 10 in the X-ray structure (marked as dot line in Figure 2b) while it extends across base pair steps from 7 to 10 in our simulations (see Figure 2B, notice that base pairs 8 and 9 are those platinated (19)). We note that this softened bending of DNA around the platinated site has recently been confirmed also experimentally (66).

The average values of the bond angles involving the platinum atom and the two N7 donor atoms in **PtDNA•noPTM** are similar to those of the X-ray structure and their standard deviations are less than 5% of such average values (Supplementary Figure S8). Hence, the bi-modal distribution of the bending angle for **PtDNA•noPTM** is not accompanied by structural changes at the cross link. Similar conclusions can be drawn for **PtDNA•A-D** (Supplementary Figure S8). In contrast, the base pairing conformations, *e.g.* shear, stretch, stagger, etc. (67), around the cross-linked base pair, experience larger fluctuations in **PtDNA•noPTM** than in **PtDNA•A-D** (Supplementary Figure S9). Also, the translations and rotations of the cross-linked base pairs (defined in literature (67)) in **PtDNA•noPTM** are larger than those in **PtDNA•A-D** (Supplementary Figure S9). All these differences are associated with greater helical rise and twist of **PtDNA•noPTM** relative to **PtDNA•A-D** (67,68). The bending in the X-ray structure was ∼47° (marked as dot line in Figure 2B) and corresponds to the bending angle of one of the two maxima (the lowest) of **PtDNA•noPTM**. We therefore suggest that **PtDNA•noPTM** samples two major conformations in aqueous solution, one similar to that identified in the solid state (19) and the other, more bent due to the helical twists, present only in water solution.

The base pairs around the cisplatin lesion in **PtDNA•A–D** undergo less conformational fluctuations than in **PtDNA•noPTM**, under the same sampling conditions (Supplementary Figure S9). In addition, the RMSF of the whole **PtDNA** is smaller in all the PTM complexes than in **noPTM** (Supplementary Table S3). These results demonstrate that the structural stability of both the protein and **PtDNA** are improved after PTMs.

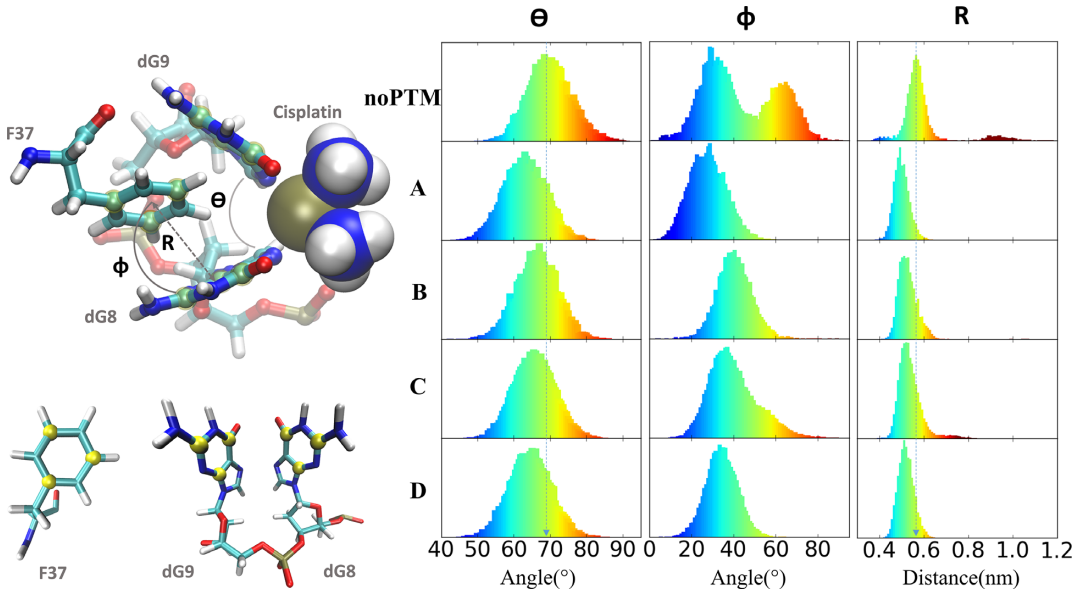

Figure 3. Left, top: Geometrical parameters **θ**, **Φ**, and **R** describing the F37 stacking configuration in the notch formed by the platinated nucleobases dG8*-dG9*. Left, bottom: The planes of the rings, used to define the three parameters, are defined by the carbon atoms shown in yellow. Right: distributions of the values of the geometrical parameters in the simulations presented here.

PtDNA-protein contacts

Nature of the intermolecular contacts. π-stacking (STC) and Van der Waals (VWC) contacts constitute altogether $>\frac{3}{4}$ of the **PtDNA**-protein contacts across all adducts (Supplementary Table S4) with STC involving mainly F37 and Y15 (Supplementary Figure S10). Direct and water-mediated hydrogen bonds (HBC), along with salt bridges, contribute by 15–19%, 5–7% and ∼1%, respectively (Supplementary Tables S4 and S5 and Supplementary Figures S10 and S11).

Overall, the nature of the contacts (and hence the percentage of VWC, STC, and HBC) changes significantly on passing from **noPTM** to **A–D** (Supplementary Figure S10). Most of the PTMs are involved in direct HBC and/or VWC with **PtDNA** (highlighted by color bands in Supplementary Figure S10). In contrast, PTMs on K29, S52, K54, K58 and K75 are water-exposed. A description of the energetics associated with these interactions (Supplementary Figure S12), as calculated with the non-bonded terms of the force field, is presented in the SI.

Mobility of the protein and in particular of the 'hydrophobic anchor' F37. Lippard and co-workers, in their seminal work on the platinated DNA/HMGB1 complex structure (19), as well as Furuita et al. (69), have identified the key structural determinant for platinated DNA/HGMB1 binding. This is the stacking configuration of the F37 side-chain inside the platinated guanines' cavity (see Figure 3). Important contributions to the stacking interaction between F37 and the cross-linked G bases include: (A) the stacking between the aromatic rings and (B) the interaction between the hydrogen atom of the phenyl in *para* position and the centroid of an aromatic ring of the guanine (13). These authors concluded that tighter is the stacking, stronger the binding (19). Indeed, the strength of the binding of the HMGB1 box-A to a platinated DNA is highly sensitive to the local structure of this notch (69).

Several structural properties (Figure 3), such as the opening of the cross-linked guanines (dG8*-dG9*) (**θ**), the stacking angle between F37 and dG8* rings (**Φ**) and the distance between F37 side-chain and dG8* (**R**), may be used to characterize this stacking configuration (69). **Φ** turns out to spread by over 80° in **noPTM**, while it is 60° or less in **A–D**. **R** distribution is broader in **noPTM** than in **A–D** (Figure 3). This is due, at least in part, to the larger rearrangements experienced by the F37 ring in **noPTM** (Supplementary Figure S13). **θ** is wider in **noPTM** (∼68°) than in **A–D** (∼63°, see Figure 3). The analysis of all these geometrical parameters indicates that F37 stacking is tighter in **A–D** than in **noPTM**. Hence, **A–D** binding can well be stronger than that of **noPTM**, consistent with the experimental result that isoforms **A-D** globally bind with higher affinity (dissociation constant, K_d = 50 nM (22)) than **noPTM** (K_d = 120 nM (70)).

Our discussion of the energetics complements our previous work on **noPTM** where the calculations reproduced quantitatively the experimental binding free energy for **noPTM** (71). To further substantiate the qualitative considerations of isoforms **A–D** made above, one could calculate the binding free energies for **A–D**, taken singularly. However, such calculation is expected, from one hand, to be highly expensive and requiring special allocations of resources, as in our previous study (71), and, from the other hand, be inconclusive at this stage because we do not know the contribution of each species to the measured value of 50 nM for isoforms **A–D** taken globally (22).

Synchrony of contacts

Our calculations have shown that the nature of the contacts changes significantly on passing from **noPTM** to **A–**

D. Moreover, PTMs also cause decreased mobility of several regions of the protein (including the hydrophobic anchor F37, which highly contributes to this specific binding) and of the **PtDNA** helical parameters around the platinum lesion, including a smaller opening of the notch with consequent decrease of the dG8*–F37 distance. To understand the cooperativity of the changes of individual contact domains between the protein and the **PtDNA** upon the overall effect of multisite PTMs, we introduced a novel concept, the *synchrony of all the intermolecular contacts*. The latter quantifies the interactions between platinated DNA and protein that occur simultaneously.

The starting point of our discussion is the so-called 'synchronic network', which describes the relationship among protein residues whose contacts with **PtDNA** occur simultaneously during the simulation (for the formal definition of subsequent concepts and quantities, see the Method section). The synchronic network is made of several 'synchronic subgroups', since not all residues are synchronous to a single node of the network. The degree of synchrony of the whole network (the 'synchrony index') ranges from 0, in the case of a fully asynchronic network, to 1, in the case of a fully synchronic network. Hence, larger the value of the synchrony index, greater the probability of forming synchronic contacts.

The **PtDNA•noPTM** network consists of four multi-residue subgroups (Y15, K89, F88, and P80) and two single-residue subgroups (M0 and S38) (Figure 4A). The subgroups consist of residues in the box-region, the N'-tail and the box-linker. This is also shown in a cartoon view of the complex 3D structure (Figure 4A) in which the amino acids are colored as the subgroup to which they belong. The intermolecular contacts associated to different subgroups are asynchronous to each other (Supplementary Figures S14 and S15). The subgroup of the box-region (including F37) accounts for ∼66% of the overall contacts (Supplementary Table S6).

Unlike the **noPTM** case, the **PtDNA•A–D** networks consist mostly of only one multi-residue subgroup (Figure 4B–E), accounting for as much as 85–93% of the contacts (Supplementary Table S6). These involve both the box-region and the termini of the protein (Figure 4B–E). In the **PtDNA•A-D** networks, three to five residues bearing PTMs (a site bearing PTM is indicated as $\mathbf{S}_{\mathrm{PTM}}$) out of six to nine $\mathbf{S}_{\mathrm{PTM}}$ are in this subgroup, indicating that several PTM-bearing residues contribute directly to the single synchronic subgroup.

We conclude that, unlike the **noPTM** case, almost all residues in the **A–D** complexes form synchronic contacts (comprising the stacking contacts of F37) with platinated DNA.

The degree of synchrony of the whole contacts network is measured by the network 'synchrony index': larger is the index, larger is the synchrony of all residues contact with **PtDNA** on average (see Materials and Methods). Consistently, the calculated network synchrony index is 0.73, 0.84, 0.89, 0.96 and 0.92 for **PtDNA•noPTM** and **PtDNA•A–D**, respectively. Figure 5A shows that the index turns out to correlate well with the fluctuations of a key descriptor of the local structure of the cross-linked guanines (**θ,** defined above). The larger are the fluctuations of **θ**, the larger the structural fluctuations of the notch, and hence the weaker the DNA/protein binding (19,69). This correlation provides a quantitative link between synchrony property and the key binding structure which determines the thermodynamic stability of the complex.

The synchrony index turns out to correlate also fairly well with the change of conformational entropy upon binding (Figure 5B). This has been calculated using the quasi-harmonic approximation (55), see Materials and Methods. Our findings therefore suggest that higher is the synchrony of the interactions, higher is the entropic cost. This entropic cost may be overcome by other contributions, such as the entropic gain of the solvent and of the counterions and/or the enthalpic gain associated with the platinated DNA/protein binding (72–74). Indeed, we have found that higher is the synchrony index, larger is the decrease of entropy associated with the binding process but tighter is the binding at the notch.

We next investigated the conformational properties of the protein isoforms **noPTM** and **A–D** in water solution in the free state. We find that as many as 73%, 99%, 73% and 98% of the residues of **noPTM** exhibit larger RMSF values than **A**, **B**, **C** and **D,** respectively (Supplementary Figure S16). This points to larger fluctuations of the proteins in the free state in water solution in the absence of PTM. Hence, we may expect that higher is the conformational rigidity of the protein in the free state, higher is the synchrony of contacts in the formation of the complex. We conclude that the increase in synchrony associated with the presence of PTMs may originate, at least in part, from an increase of conformational rigidity of the proteins in the free state in water solution upon formation of the PTMs.

Overall, **PtDNA•A–D** feature significant differences with respect to **PtDNA•noPTM**. Moreover, isoforms **PtDNA•A–D** were the major components isolated in *in vivo* conditions (22), thus it is likely that **PtDNA•noPTM** does not play a dominant role in the specific case of platinum drugs. However, the multiple conformations of **noPTM** witness the ability of the protein to undergo structural changes, consequent to PTMs, allowing it to perform specific tasks on request.

CONCLUDING REMARKS

Although the PtDNA/HMGB1 complex is not the sole arbiter of cisplatin cytotoxicity (75–78), its well thermodynamic and structural characterization has provided a benchmark for the application of theoretical approaches to a better understanding of intermolecular recognition processes. Here, we have investigated the impact of multisite PTMs of HMGB1 isoforms occurring *in vivo* upon the formation of platinated DNA/HMGB1 complexes at atomistic level. The PTM patterns analyzed in the present case (Table 1) are those sorted out from a cellular milieu using a Pt-cross-linked DNA as a probe (22). Acetylation of lysines and phosphorylation of serines both reduce the positive charges on the HMGB1 protein, hence one may expect diminished electrostatic attraction for negatively charged DNA; (34,35) however, PTMs were experimentally found to increase the binding affinity of the **PtDNA•**protein complex (22). Our simulation suggests that the reduction of

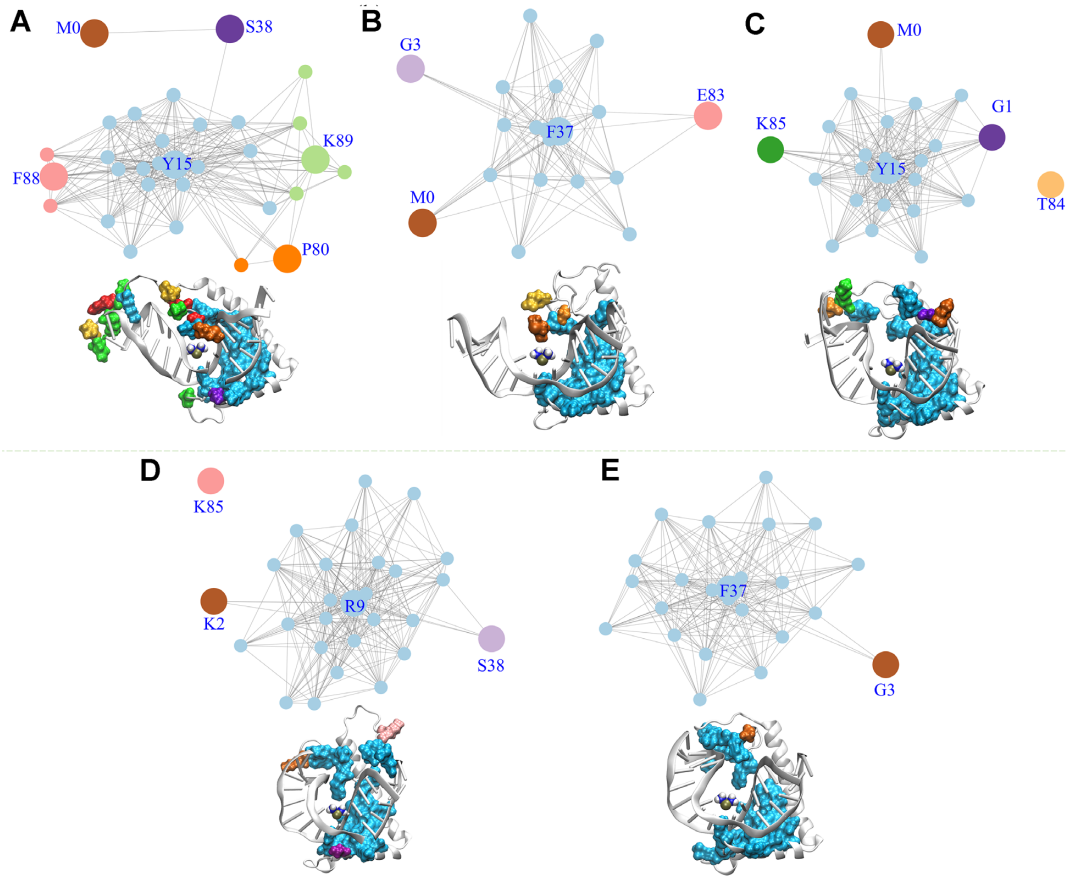

Figure 4. Synchronic networks for **noPTM** (**A**), **A** (**B**), **B** (**C**), **C** (**D**) and **D** (**E**) complexes. The residues belonging to the different synchronic subgroups of each network are displayed also in 3D structure.

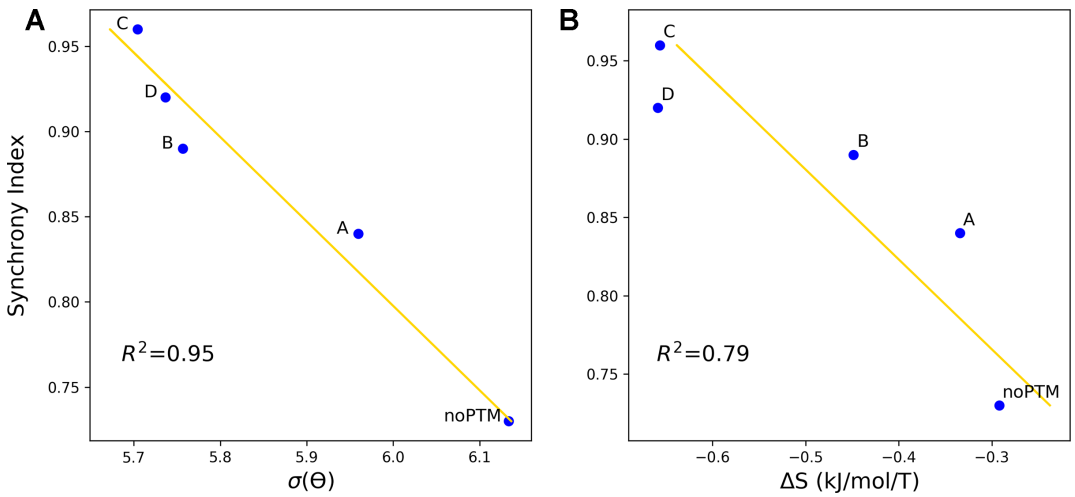

Figure 5. Correlations between the synchrony indexes and: (**A**) the fluctuations of **θ**, expressed here as standard deviation of the distribution of values during the simulations, σ(**θ**); (**B**) the conformational entropy of binding (ΔS), calculated using the quasi-harmonic approximation (55). The calculated values are shown as blue dots, the linear fit as a gold line. The R^2 values are also reported.

positive charges, consequent to lysine acetylation and serine phosphorylation, affects the nature of nonbonded contacts on passing from **PtDNA●noPTM** to **PtDNA●A–D**. The hydrophobic contacts constitute altogether $> \frac{3}{4}$ of the intermolecular contacts in all cases (Supplementary Table S3), while direct and water-mediated hydrogen bonds vary from 15 to 19% and from 5% to 7%, respectively. The change of these contacts can indeed affect the energetics of **PtDNA●**protein interactions (Supplementary Figure S12).

Interestingly, our calculations also showed that the occurrence of PTMs turns out to decrease the apparent flexibility of the hydrophobic anchor F37 sandwiched by the two cross-linked guanines. The stability of this hydrophobic binding is known to be a key element of the binding affinity between the protein and platinated DNA (19,69). Our simulation results are in line with the experimental findings that overall, **A–D** bind to **PtDNA** with higher affinity than **noPTM** (22): indeed, the F37 stacking is stronger in **A–D** than in **noPTM** (Figure 3).

Besides the F37, other two separate domains of the protein, the protein terminal loops, are also much less flexible in **PtDNA●A–D** than in **PtDNA●noPTM**. This is due, at least in part, to the inherent higher structural rigidity on passing from **noPTM** to **A–D** in water solution.

To identify a link between the structural rigidity of the protein terminal loops and the better fitting between the F37 and the two cross-linked guanines in **A–D**, we defined a mathematical quantity which monitors the synchrony in the formation of all the intermolecular contacts between protein and **PtDNA**. The degree of synchrony of the protein–**PtDNA** interactions, which is characterized in this work by synchronic networks and synchrony indexes, were significantly increased for all the four PTM isoforms. High synchrony of the protein–**PtDNA** contacts requires better collectivity or cooperativity of these individual contact domains, which means that the overall protein–**PtDNA** interfaces are more stable after PTMs. Moreover, we observed a fair anti-correlation between the fluctuation of the descriptor of the key binding site F37 and the synchrony index. The latter characterizes the synchrony of the protein–**PtDNA** interface globally. Therefore, the stabilized binding of F37 on the interface is due to better synchrony of all the contacts regulated by the PTMs. The synchrony analysis represents a different, independent, and valuable point of view to investigate standard thermodynamic variables such as the configurational entropy or the binding free energy. In addition, it is a convenient way to show interface contacts' cooperativity (Figure 4) and conformational flexibility (Figure 5). Both aspects do not emerge from other types of analysis. Thus, it is possible to conclude that the synchrony analysis represents a new tool to investigate intermolecular recognition processes.

In summary, our study on the PTMs of HMGB1-**PtDNA** complexes reveals that a collective behavior of multisite PTMs can contribute to stabilize the key contact between the F37 and the cross-linked site of **PtDNA**. This in turn may contribute to the experimentally observed increasing of binding affinity of the complexes on passing from **noPTM** to **A–D**.

SUPPORTING INFORMATION

Clustering analysis, secondary structures, RMSD, RMSF of the proteins; RMSF, RMSD, helix axes subtending angle, bond angles around the platinate atom, helical parameters of the **PtDNA**; intermolecular contacts, water-mediated hydrogen bond contacts between the protein and **PtDNA**; homology modeling, MD parameters, simulation, other technical details of analyses employed in this work, and the energetics of the intermolecular contacts.

SUPPLEMENTARY DATA

Supplementary Data are available at NAR Online.

ACKNOWLEDGEMENTS

The authors gratefully acknowledge the computing time granted on the supercomputer JUQUEEN at Jülich Supercomputing Centre (JSC).

FUNDING

Horizon 2020 research and innovation program of the European Commission under the Marie Sklodowska-Curie Grant Agreement [642069 to W.L., P.C., G.R.]; National Natural Science Foundation of China [21505134 to W.L.]; F.A. and G.N. thank the University of Bari and the Consorzio Interuniversitario di Ricerca in Chimica dei Metalli nei Sistemi Biologici (CIRCMSB) for support. Funding for open access charge: Horizon 2020 research and innovation program of the European Commission under the Marie Sklodowska-Curie Grant Agreement [642069].
Conflict of interest statement. None declared.

REFERENCES

1. Johnstone,T.C., Suntharalingam,K. and Lippard,S.J. (2016) The next generation of platinum drugs: targeted Pt(II) agents, nanoparticle delivery, and Pt(IV) prodrugs. *Chem. Rev.*, **116**, 3436–3486.
2. Hannon,M.J. and Reedijk,J. (2015) Metal interactions with nucleic acids. *Dalton Trans.*, **44**, 3503–3504.
3. Gibson,D. (2009) The mechanism of action of platinum anticancer agents–what do we really know about it? *Dalton Trans.*, **48**, 10681–10689.
4. Muhammad,N. and Guo,Z. (2014) Metal-based anticancer chemotherapeutic agents. *Curr. Opin. Chem. Biol.*, **19**, 144–153.
5. Spreckelmeyer,S., Estrada-Ortiz,N., Prins,G.G.H., van der Zee,M., Gammelgaard,B., Sturup,S., de Graaf,I.A.M., Groothuis,G.M.M. and Casini,A. (2017) On the toxicity and transport mechanisms of cisplatin in kidney tissues in comparison to a gold-based cytotoxic agent. *Metallomics*, **9**, 1786–1795.
6. Galluzzi,L., Senovilla,L., Vitale,I., Michels,J., Martins,I., Kepp,O., Castedo,M. and Kroemer,G. (2012) Molecular mechanisms of cisplatin resistance. *Oncogene*, **31**, 1869–1883.
7. Pillozzi,S., D'Amico,M., Bartoli,G., Gasparoli,L., Petroni,G., Crociani,O., Marzo,T., Guerriero,A., Messori,L., Severi,M. *et al.* (2018) The combined activation of KCa3.1 and inhibition of Kv11.1/hERG1 currents contribute to overcome cisplatin resistance in colorectal cancer cells. *Br. J. Cancer*, **118**, 200–212.
8. Wood,R.D., Araujo,S.J., Ariza,R.R., Batty,D.P., Biggerstaff,M., Evans,E., Gaillard,P.H., Gunz,D., Koberle,B., Kuraoka,I. *et al.* (2000) DNA damage recognition and nucleotide excision repair in mammalian cells. *Cold Spring Harb. Symp. Quant. Biol.*, **65**, 173–182.
9. Pil,P.M. and Lippard,S.J. (1992) Specific binding of chromosomal protein-Hmg1 to DNA damaged by the anticancer drug cisplatin. *Science*, **256**, 234–237.

10. Eastman,A. (1987) The formation, isolation and characterization of DNA adducts produced by anticancer platinum complexes. *Pharmacol. Therapeut.*, **34**, 155–166.
11. Fichtingerschepman,A.M.J., Vanderveer,J.L., Denhartog,J.H.J., Lohman,P.H.M. and Reedijk,J. (1985) Adducts of the antitumor drug Cis-Diamminedichloroplatinum(Ii) with DNA - formation, identification, and quantitation. *Biochemistry*, **24**, 707–713.
12. Yusein-Myashkova,S., Ugrinova,I. and Pasheva,E. (2016) Non-histone protein HMGB1 inhibits the repair of cisplatin damaged DNA in NIH-3T3 murine fibroblasts. *BMB Rep.*, **49**, 99–104.
13. Park,S. and Lippard,S.J. (2012) Binding interaction of HMGB4 with Cisplatin-Modified DNA. *Biochemistry*, **51**, 6728–6737.
14. Oliver,T.G., Mercer,K.L., Sayles,L.C., Burke,J.R., Mendus,D., Lovejoy,K.S., Cheng,M.H., Subramanian,A., Mu,D., Powers,S. *et al.* (2010) Chronic cisplatin treatment promotes enhanced damage repair and tumor progression in a mouse model of lung cancer. *Genes Dev.*, **24**, 837–852.
15. Awuah,S.G., Riddell,I.A. and Lippard,S.J. (2017) Repair shielding of platinum-DNA lesions in testicular germ cell tumors by high-mobility group box protein 4 imparts cisplatin hypersensitivity. *Proc. Natl. Acad. Sci. U.S.A.*, **114**, 950–955.
16. Kasparkova,J., Marini,V., Najajreh,Y., Gibson,D. and Brabec,V. (2003) DNA binding mode of the cis and trans geometries of new antitumor nonclassical platinum complexes containing piperidine, piperazine, or 4-picoline ligand in cell-free media. Relations to their activity in cancer cell lines. *Biochemistry*, **42**, 6321–6332.
17. Malina,J., Novakova,O., Vojtiskova,M., Natile,G. and Brabec,V. (2007) Conformation of DNA GG intrastrand cross-link of antitumor oxaliplatin and its enantiomeric analog. *Biophys. J.*, **93**, 3950–3962.
18. Kasparkova,J., Vojtiskova,M., Natile,G. and Brabec,V. (2008) Unique properties of DNA interstrand cross-links of antitumor oxaliplatin and the effect of chirality of the carrier ligand. *Chem.-Eur. J.*, **14**, 1330–1341.
19. Ohndorf,U.M., Rould,M.A., He,Q., Pabo,C.O. and Lippard,S.J. (1999) Basis for recognition of cisplatin-modified DNA by high-mobility-group proteins. *Nature*, **399**, 708–712.
20. Kasparkova,J., Delalande,O., Stros,M., Elizondo-Riojas,M.A., Vojtiskova,M., Kozelka,J. and Brabec,V. (2003) Recognition of DNA interstrand cross-link of antitumor cisplatin by HMGB1 protein. *Biochemistry*, **42**, 1234–1244.
21. Malarkey,C.S. and Churchill,M.E.A. (2012) The high mobility group box: the ultimate utility player of a cell. *Trends Biochem. Sci.*, **37**, 553–562.
22. He,Y.F., Ding,Y., Wang,D., Zhang,W.J., Chen,W.Z., Liu,X.C., Qin,W.J., Qian,X.H., Chen,H. and Guo,Z.J. (2015) HMGB1 bound to cisplatin–DNA adducts undergoes extensive acetylation and phosphorylation in vivo. *Chem. Sci.*, **6**, 2074–2078.
23. Ugrinova,I., Pasheva,E.A., Armengaud,J. and Pashev,I.G. (2001) In vivo acetylation of HMG1 protein enhances its binding affinity to distorted DNA structures. *Biochemistry*, **40**, 14655–14660.
24. Ugrinova,I., Mitkova,E., Moskalenko,C., Pashev,I. and Pasheva,E. (2007) DNA bending versus DNA end joining activity of HMGB1 protein is modulated in vitro by acetylation. *Biochemistry*, **46**, 2111–2117.
25. Assenberg,R., Webb,M., Connolly,E., Stott,K., Watson,M., Hobbs,J. and Thomas,J.O. (2008) A critical role in structure-specific DNA binding for the acetylatable lysine residues in HMGB1. *Biochem. J.*, **411**, 553–561.
26. Topalova,D., Ugrinova,I., Pashev,T.G. and Pasheva,E.A. (2008) HMGB1 protein inhibits DNA replication in vitro: a role of the acetylation and the acidic tail. *Int. J. Biochem Cell B*, **40**, 1536–1542.
27. Elenkov,I., Pelovsky,P., Ugrinova,I., Takahashi,M. and Pasheva,E. (2011) The DNA binding and bending activities of truncated tail-less HMGB1 protein are differentially affected by Lys-2 and Lys-81 residues and their acetylation. *Int. J. Biol. Sci.*, **7**, 691–699.
28. Kang,R., Chen,R., Zhang,Q., Hou,W., Wu,S., Cao,L., Huang,J., Yu,Y., Fan,X.G., Yan,Z. *et al.* (2014) HMGB1 in health and disease. *Mol. Aspects Med.*, **40**, 1–116.
29. Walsh,C.T., Garneau-Tsodikova,S. and Gatto,G.J. (2005) Protein posttranslational modifications: the chemistry of proteome diversifications. *Angew. Chem. Int. Ed.*, **44**, 7342–7372.
30. Prabakaran,S., Lippens,G., Steen,H. and Gunawardena,J. (2012) Post-translational modification: nature's escape from genetic imprisonment and the basis for dynamic information encoding. *Wires Syst. Biol. Med.*, **4**, 565–583.
31. Petrov,D., Margreitter,C., Grandits,M., Oostenbrink,C. and Zagrovic,B. (2013) A systematic framework for molecular dynamics simulations of protein post-translational modifications. *PLoS Comput. Biol.*, **9**, e1003154.
32. Ikebe,J., Sakuraba,S. and Kono,H. (2016) H3 histone tail conformation within the nucleosome and the impact of K14 acetylation studied using enhanced sampling simulation. *PLoS Comput. Biol.*, **12**, e1004788.
33. Winogradoff,D., Echeverria,I., Potoyan,D.A. and Papoian,G.A. (2015) The acetylation landscape of the H4 histone tail: disentangling the interplay between the specific and cumulative effects. *J. Am. Chem. Soc.*, **137**, 6245–6253.
34. Di Cerbo,V., Mohn,F., Ryan,D.P., Montellier,E., Kacem,S., Tropberger,P., Kallis,E., Holzner,M., Hoerner,L., Feldmann,A. *et al.* (2014) Acetylation of histone H3 at lysine 64 regulates nucleosome dynamics and facilitates transcription. *Elife*, **3**, 01632.
35. Chang,L. and Takada,S. (2016) Histone acetylation dependent energy landscapes in tri-nucleosome revealed by residue-resolved molecular simulations. *Sci. Rep.*, **6**, 34441.
36. Wan,F.Y. and Lenardo,M.J. (2009) Specification of DNA binding activity of NF-kappa B proteins. *CSH Perspect. Biol.*, **1**, a000067.
37. Oeckinghaus,A. and Ghosh,S. (2009) The NF-kappa B family of transcription factors and its regulation. *CSH Perspect. Biol.*, **1**, a000034.
38. Fenollar-Ferrer,C., Anselmi,C., Carnevale,V., Raugei,S. and Carloni,P. (2012) Insights on the acetylated NF-kappaB transcription factor complex with DNA from molecular dynamics simulations. *Proteins*, **80**, 1560–1568.
39. Moghadam,M.E., Saidifar,M., Rostami-Charati,F., Ajloo,D. and Ghadamgahi,M. (2014) Molecular dynamic simulation and spectroscopic investigation of some cytotoxic Palladium(II) complexes interaction with human serum albumin. *Comb. Chem. High Trans. Scr.*, **17**, 781–789.
40. Palermo,G., Magistrato,A., Riedel,T., von Erlach,T., Davey,C.A., Dyson,P.J. and Rothlisberger,U. (2016) Fighting cancer with transition metal complexes: From naked DNA to protein and chromatin targeting strategies. *ChemMedChem*, **11**, 1199–1210.
41. Parker,L.J., Italiano,L.C., Morton,C.J., Hancock,N.C., Ascher,D.B., Aitken,J.B., Harris,H.H., Campomanes,P., Rothlisberger,U., De Luca,A. *et al.* (2011) Studies of glutathione transferase P1-1 bound to a platinum(IV)-based anticancer compound reveal the molecular basis of its activation. *Chemistry*, **17**, 7806–7816.
42. Vargiu,A.V., Robertazzi,A., Magistrato,A., Ruggerone,P. and Carloni,P. (2008) The hydrolysis mechanism of the anticancer ruthenium drugs NAMI-A and ICR investigated by DFT-PCM calculations. *J. Phys. Chem. B*, **112**, 4401–4409.
43. Gossens,C., Tavernelli,I. and Rothlisberger,U. (2008) DNA structural distortions induced by ruthenium-arene anticancer compounds. *J. Am. Chem. Soc.*, **130**, 10921–10928.
44. Adhireksan,Z., Davey,G.E., Campomanes,P., Groessl,M., Clavel,C.M., Yu,H.J., Nazarov,A.A., Yeo,C.H.F., Ang,W.H., Droge,P. *et al.* (2014) Ligand substitutions between ruthenium-cymene compounds can control protein versus DNA targeting and anticancer activity. *Nat. Commun.*, **5**, 3462
45. Vargiu,A.V. and Magistrato,A. (2014) Atomistic-Level portrayal of Drug-DNA Interplay: A history of courtships and meetings revealed by molecular simulations. *ChemMedChem*, **9**, 1966–1981.
46. Wang,J., Cieplak,P. and Kollman,P.A. (2000) How well does a restrained electrostatic potential (RESP) model perform in calculating conformational energies of organic and biological molecules? *J. Comput. Chem.*, **21**, 1049–1074.
47. Lindorff-Larsen,K., Piana,S., Palmo,K., Maragakis,P., Klepeis,J.L., Dror,R.O. and Shaw,D.E. (2010) Improved side-chain torsion potentials for the Amber ff99SB protein force field. *Proteins Struct. Funct. Bioinf.*, **78**, 1950–1958.
48. Hornak,V., Abel,R., Okur,A., Strockbine,B., Roitberg,A. and Simmerling,C. (2006) Comparison of multiple amber force fields and development of improved protein backbone parameters. *Proteins-Struct. Funct. Bioinformatics*, **65**, 712–725.
49. Ivani,I., Dans,P.D., Noy,A., Perez,A., Faustino,I., Hospital,A., Walther,J., Andrio,P., Goni,R., Balaceanu,A. *et al.* (2016) Parmbsc1: a refined force field for DNA simulations. *Nat. Methods*, **13**, 55–58.

50. Wang,L., Friesner,R.A. and Berne,B.J. (2011) Replica exchange with solute scaling: a more efficient version of replica exchange with solute tempering (REST2) (vol 115, pg 9431, 2011). *J. Phys. Chem. B*, **115**, 11305–11305.
51. Lavery,R., Moakher,M., Maddocks,J.H., Petkeviciute,D. and Zakrzewska,K. (2009) Conformational analysis of nucleic acids revisited: Curves+. *Nucleic. Acids. Res.*, **37**, 5917–5929.
52. McDonald,I.K. and Thornton,J.M. (1994) Satisfying hydrogen bonding potential in proteins. *J. Mol. Biol.*, **238**, 777–793.
53. Luscombe,N.M., Laskowski,R.A. and Thornton,J.M. (1997) NUCPLOT: a program to generate schematic diagrams of protein-nucleic acid interactions. *Nucleic Acids Res.*, **25**, 4940–4945.
54. Karplus,M. and Kushick,J.N. (1981) Method for estimating the configurational entropy of macromolecules. *Macromolecules*, **14**, 325–332.
55. Frederick,K.K., Marlow,M.S., Valentine,K.G. and Wand,A.J. (2007) Conformational entropy in molecular recognition by proteins. *Nature*, **448**, 325–U323.
56. Karplus,M., Ichiye,T. and Pettitt,B.M. (1987) Configurational entropy of native proteins. *Biophys. J.*, **52**, 1083–1085.
57. An,G.Z. (1988) A note on the cluster variation method. *J. Stat. Phys.*, **52**, 727–734.
58. Frey,B.J. and Dueck,D. (2007) Clustering by passing messages between data points. *Science*, **315**, 972–976.
59. Kiers,H.A.L. (1999) Modern multidimensional scaling: theory and applications. *Psychometrika*, **64**, 95–97.
60. Kruskal,J.B. (1964) Nonmetric Multidimensional-scaling - a numerical-method. *Psychometrika*, **29**, 115–129.
61. Sireci,S.G. (2003) Modern multidimensional scaling: theory and applications. *J. Educ. Meas.*, **40**, 277–280.
62. Lavery,R. and Sklenar,H. (1988) The definition of generalized helicoidal parameters and of axis curvature for irregular nucleic acids. *J. Biomol. Struct. Dyn.*, **6**, 63–91.
63. Widom,J. (1984) Molecular-biology - DNA bending and kinking. *Nature*, **309**, 312–313.
64. Saenger,W. (1984) In: Cantor,CR (ed). *Principles of Nucleic Acid Structure*. Springer-Verlag, NY, pp. 51–104.
65. Kozelka,J., Petsko,G.A., Quigley,G.J. and Lippard,S.J. (1986) High-salt and low-salt models for kinked adducts of cis-diamminedichloroplatinum(Ii) with oligonucleotide duplexes. *Inorg. Chem.*, **25**, 1075–1077.
66. Dutta,S., Rivetti,C., Gassman,N.R., Young,C.G., Jones,B.T., Scarpinato,K. and Guthold,M. (2018) Analysis of single, cisplatin-induced DNA bends by atomic force microscopy and simulations. *J. Mol. Recognit.*, **31**, e2731.
67. Blanchet,C., Pasi,M., Zakrzewska,K. and Lavery,R. (2011) CURVES plus web server for analyzing and visualizing the helical, backbone and groove parameters of nucleic acid structures. *Nucleic Acids Res.*, **39**, W68–W73.
68. Richmond,T.J. and Davey,C.A. (2003) The structure of DNA in the nucleosome core. *Nature*, **423**, 145–150.
69. Furuita,K., Murata,S., Jee,J.G., Ichikawa,S., Matsuda,A. and Kojima,C. (2011) Structural feature of bent DNA recognized by HMGB1. *J. Am. Chem. Soc.*, **133**, 5788–5790.
70. Jung,Y. and Lippard,S.J. (2003) Nature of full-length HMGB1 binding to cisplatin-modified DNA. *Biochemistry*, **42**, 2664–2671.
71. Nguyen,T.H., Rossetti,G., Arnesano,F., Ippoliti,E., Natile,G. and Carloni,P. (2014) Molecular recognition of platinated DNA from chromosomal HMGB1. *J. Chem. Theory Comput.*, **10**, 3578–3584.
72. Zhou,H.X. and Gilson,M.K. (2009) Theory of free energy and entropy in noncovalent binding. *Chem. Rev.*, **109**, 4092–4107.
73. Kalodimos,C.G., Biris,N., Bonvin,A.M., Levandoski,M.M., Guennuegues,M., Boelens,R. and Kaptein,R. (2004) Structure and flexibility adaptation in nonspecific and specific protein-DNA complexes. *Science*, **305**, 386–389.
74. Pabo,C.O. and Sauer,R.T. (1984) Protein-DNA recognition. *Annu. Rev. Biochem.*, **53**, 293–321.
75. Casini,A. and Reedijk,J. (2012) Interactions of anticancer Pt compounds with proteins: an overlooked topic in medicinal inorganic chemistry? *Chem. Sci.*, **3**, 3135–3144.
76. Mezencev,R. (2014) Interactions of cisplatin with non-DNA targets and their influence on anticancer activity and drug toxicity: The complex world of the platinum complex. *Curr. Cancer Drug Tar.*, **14**, 794–816.
77. Osborn,M.F., White,J.D., Haley,M.M. and DeRose,V.J. (2014) Platinum-RNA modifications following drug treatment in S. cerevisiae identified by click chemistry and enzymatic mapping. *ACS Chem. Biol.*, **9**, 2404–2411.
78. Arnesano,F., Nardella,M.I. and Natile,G. (2018) Platinum drugs, copper transporters and copper chelators. *Coordin. Chem. Rev.*, **374**, 254–260.